JACS
JOURNAL OF THE AMERICAN CHEMICAL SOCIETY

Article

pubs.acs.org/JACS

Many-Body Effects in Nanocrystal Superlattices: Departure from Sphere Packing Explains Stability of Binary Phases

Michael A. Boles and Dmitri V. Talapin*

University of Chicago and James Franck Institute, Chicago, Illinois 60637, United States

Supporting Information

ABSTRACT: This work analyzes the role of hydrocarbon ligands in the self-assembly of nanocrystal (NC) superlattices. Typical NCs, composed of an inorganic core of radius R and a layer of capping ligands with length L, can be described as soft spheres with softness parameter L/R. Using particle tracking measurements of transmission electron microscopy images, we find that close-packed NCs, like their hard-sphere counterparts, fill space at approximately 74% density independent of softness. We uncover deformability of the ligand capping layer that leads to variable effective NC size in response to the coordination environment. This effect plays an important role in the packing of particles in binary nanocrystal superlattices (BNSLs). Measurements on BNSLs composed of NCs of varying softness in several coordination geometries indicate that NCs deform to produce dense BNSLs that would otherwise be low-density arrangements if the particles remained spherical. Consequently, rationalizing the mixing of two NC species during BNSL self-assembly need not employ complex energetic interactions. We summarize our analysis in a set of packing rules. These findings contribute to a general understanding of entropic effects during crystallization of deformable objects (e.g., nanoparticles, micelles, globular proteins) that can adapt their shape to the local coordination environment.

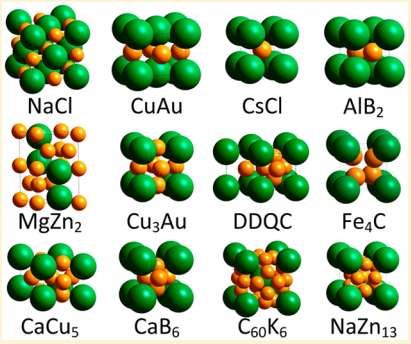

INTRODUCTION

Self-organization of monodisperse colloidal particles has been a topic of interest since the iridescence of gem opals was attributed to diffraction of light from regularly packed silica spheres.[1] Micron-sized silica or polymer beads crystallize into close-packed structures, either cubic (fcc) or hexagonal (hcp), which may be rationalized by simple sphere-packing arguments.[2] This ordering transition is driven by entropy: with negligible energetic interactions between beads, the preferred structure of the solvated colloidal crystal is one that maximizes the free volume available to individual spheres. While a disordered collection of monodisperse spheres jams at particle volume fraction $\varphi \approx 0.64$, adoption of a close-packed arrangement allows for local translations of individual particles at volume fractions as high as $\varphi \approx 0.74$. Cocrystallization of two sizes of micron-diameter spheres[3,4] has produced binary arrangements isostructural with NaCl, AlB_2, and $NaZn_{13}$ (Figure 1a). In parallel, much effort has been made to evaluate the relative stability of binary phases of hard-sphere[5−7] and soft-sphere[8,9] colloids. In the latter case, soft interactions have been treated by pair potentials. Packing geometry considerations reveal that for certain sphere radius ratios ($\gamma = R_B/R_A$, where R_B is the radius of the smaller B sphere and R_A is the radius of the larger A sphere), binary structures of micron-sized beads fill space with densities approaching or exceeding those of single-component fcc and hcp arrangements (Figure 1b). For these particles, the size ratio has excellent predictive power over the binary phase stability, confirming that efficient packing of spheres drives the system toward ordered two-component assemblies.

A new class of colloids emerged with the development of the synthesis of monodisperse semiconductor,[16] metal,[17] and metal oxide[18] nanocrystals (NCs). These nanometer-sized, solution-grown particles consist of an inorganic core and a surface-tethered surfactant shell that prevents flocculation of the NCs. Monodisperse NCs can be coaxed into adoption of ordered arrangements,[19,20] including cocrystallization of two types of particles into binary NC superlattices (BNSLs).[10,21] BNSL phases have been reported with AB, AB_2, AB_3, A_6B_{19}, AB_4, AB_5, AB_6, and AB_{13} stoichiometry and cubic, hexagonal, tetragonal, orthorhombic,[22] and dodecagonal quasicrystalline (DDQC)[13] symmetries (Figure 1a). These structures have been modeled as sphere packings with effective sphere radius R_{eff} given as the core radius plus measured effective ligand shell thickness.[10,19] In contrast to assemblies of micron-sized particles, attempts to rationalize BNSLs as efficient sphere packings using the assigned effective NC sizes and size ratios have been less fruitful. Of the 20 or so BNSL phases reported to date, most (~85%) are predicted to fill space less densely than close-packed arrangements of monodisperse hard spheres (Figure 1b). The stability of these BNSLs against phase separation into dense packings of large and small particles has remained an open question. It was suggested that a confluence of forces (electrostatic, dipolar, van der Waals) may be responsible for

Received: January 25, 2015
Published: March 16, 2015

DOI: 10.1021/jacs.5b00839
J. Am. Chem. Soc. 2015, 137, 4494−4502

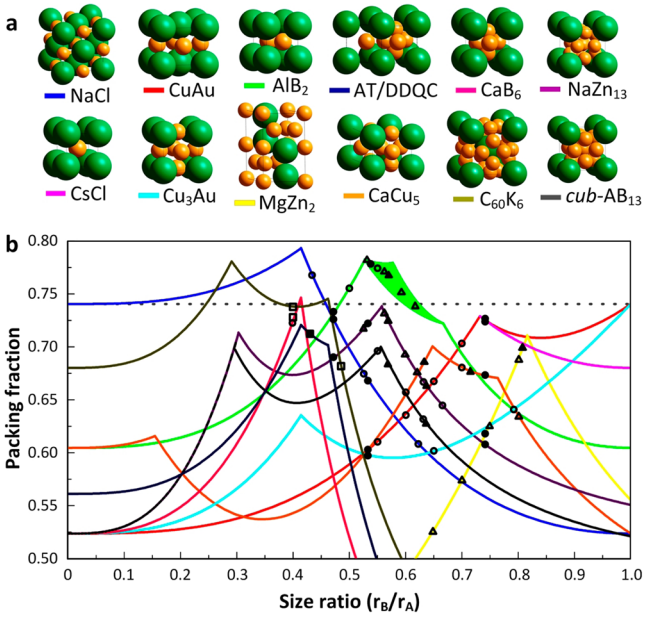

Figure 1. Structural diversity of binary nanocrystal superlattices and low packing density predictions for most observed phases. (a) Models of 12 commonly observed binary arrangements showing larger A spheres in green and smaller B spheres in orange. Unit cells with AB, AB_2, AB_3, AB_5, AB_6, and AB_{13} stoichiometry as well as the structural motifs of Archimedean tiling (AT) and dodecagonal quasicrystal (DDQC) configurations are shown. (b) Plot of density vs size ratio for spheres packed in these arrangements. Overlay: data points showing phases observed in several BNSL studies using reported effective size ratios and densities predicted using sphere-packing models. Most observed BNSLs appear to be open arrangements compared with close-packed monodisperse hard spheres (dotted line). Works cited: ○, ref 10; ●, ref 11; □, ref 12; ■, ref 13; △, ref 14; ▲, ref 15.

BNSL formation.[8,23,24] However, the growing body of literature showing the diversity of binary NC arrangements, as well as the similarity of BNSLs self-assembled from chemically different NCs, motivates our search for yet-unknown general principles that promote structural complexity of BNSLs far beyond the simple phase diagram of micron-sized spherical colloidal particles.

METHODS

Nanocrystal Synthesis and Ligand Exchange. Au NCs were made by reduction of gold(III) chloride with *tert*-butylamine–borane complex in tetrahydronaphthalene and oleylamine.[25] The Au NC core diameter was varied between ~2.5 and ~5.1 nm by adjusting the injection temperature between 40 and 2 °C, respectively. PbS NCs were made by injection of bis(trimethylsilyl)sulfide into lead(II) oleate in octadecene (ODE) and oleic acid (OA) at 150 °C.[26] The PbS NC core diameter was adjusted between ~3.0 and ~7.0 nm by varying the OA:ODE ratio. γ-Fe_2O_3 NCs were made by oxidative decomposition of iron pentacarbonyl with trimethylamine oxide in the presence of oleic acid and dioctyl ether at 120 °C.[18] All of the NCs were precipitated twice from hexane/ethanol and redispersed in hexane for storage. Ligand exchange was carried out by stirring NCs with excess displacing ligand at a 1:1 mass ratio in hexane for 2 h at room temperature. Ligand-exchanged NCs were separated from excess unbound ligands by washing twice with hexane/ethanol and then stored in tetrachloroethylene (TCE). The strong van der Waals interactions between surface-bound C_{18}-length saturated hydrocarbon chains encourages partial precipitation of octadecanethiol-capped Au and stearic acid-capped PbS NCs from storage solution over several days. Warming the NC solution to ~50 °C for a couple minutes melts the capping layer, allowing for complete redissolution of the precipitated NCs.

Nanocrystal Self-Assembly. Single-component arrays of Au, PbS, and Fe_2O_3 NCs were prepared by drop-casting 10 μL of NC solution in TCE onto transmission electron microscopy (TEM) carbon supports resting on filter paper placed upon a hot plate set to 50 °C. The NC array thickness was tuned from submonolayer to multilayer coverage by adjusting the drop-cast solution concentration within the range 0.2–2 mg/mL. Drop-casting at room temperature reduced the degree of ordering of NC arrays compared with drop-casting at 50 °C. BNSLs were assembled by evaporation of a two-component NC solution at 50 °C and ~0.5 atm over TEM grids tilted ~25° from horizontal.[11] Assembly solutions contained on the order of 0.1 mg of each NC component in 20 μL of octane. Variation of the concentration ratio of NC components was found to influence the relative abundance of BNSL structures with different stoichiometries (e.g., AB vs AB_{13}).

Measurement of Interparticle Separations. Single-component and binary NC arrays were imaged on an FEI Technai F30 transmission electron microscope operating at an accelerating voltage of 300 kV. Tilting experiments with a dual-axis sample holder allowed for clear assignment of the BNSL structure and extraction of the lattice parameter oriented perpendicular to the carbon support. The curvature of Archimedean tiling (AT) and DDQC BNSL domains prevented measurement of the *c* axis. Small- and wide-angle electron diffraction (SAED and WAED, respectively) patterns were collected from ~0.1 μm^2-sized BNSL areas. TEM images of NC arrays were analyzed using a MATLAB particle tracking code. Image noise was reduced with Gaussian filter, and particle centers were assigned on the basis of a weighted average of pixel intensities within the NC core. Delaunay triangulation of NC centers produced a set of bonds whose lengths were used to estimate the effective NC size. Coordination numbers of NCs were calculated by counting the number of centroids falling within two standard deviations of the distribution maximum. Comparison of core diameters for various coordination numbers was made by using Roberts edge detection algorithm to trace NC core perimeter, filling the interior of the trace to create a blob, and extracting an equivalent diameter from the blob area. Batch measurement of 25 TEM images of single-component arrays allowed for analysis of a large data set (10^4–10^5 bond counts). The statistical significance of variations in effective particle size was evaluated by assigning *P* values to measured separations in single-component and binary arrays (see Tables S2 and S5 in the Supporting Information).

RESULTS

Here we investigate the structure of surface ligands within single-component and binary NC arrays and analyze their role in directing the unique phase behavior observed for such particles. Surface ligands, typically hydrocarbon chains tethered to the NC surface through a headgroup linker, collectively form a soft corona around the particle. The ratio of the extended chain length (L) to the core radius (R) can be used as a measure of particle softness and a means of differentiation between colloidal NCs ($L/R \sim 1$) and typical micron-sized colloidal beads ($L/R \sim 0.01$). The interactions between surface ligands are repulsive in a good solvent (e.g., hexane) but attractive in vacuum (e.g., a dry superlattice). During self-assembly, solvent evaporation acts to densify the NC solution, forcing solvated particles into contact with one another. Complete removal of the solvent freezes the collection of NCs into a superlattice with dimensions set by the balance between ligand elastic repulsion and van der Waals attraction forces.

We chose software analysis of TEM images to collect information on NC surface ligand structure. While infrared (IR) spectroscopy can be used for detailed reconstruction of hydrocarbon structure in highly ordered systems (e.g.,

DOI: 10.1021/jacs.5b00839
J. Am. Chem. Soc. 2015, 137, 4494–4502

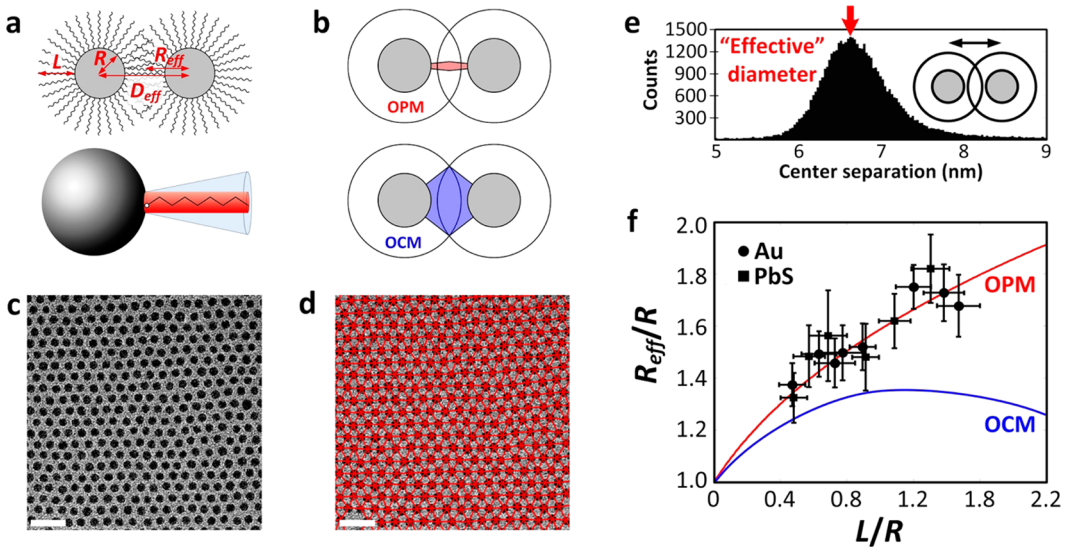

Figure 2. Geometric models for soft particle contact and measurement of separations in Au and PbS monolayer arrays. (a) Sketch of NC contact with labeled core radius, ligand length, effective NC radius, and diameter (top) and geometric reduction of the NC, ligand, and excess volume to a sphere, cylinder, and cone, respectively (bottom). (b) Sketch of hydrocarbon space-filling assumptions made by two models of ligand packing in NC arrays. See the main text for explanation. (c, d) Particle tracking analysis of TEM images allows for collection of experimental interparticle separation statistics. A sample area of a monolayer of 4.1 nm Au NCs capped with octadecanethiol ligands is shown. Scale bars are 20 nm. (e) Effective NC diameter, including core and ligand contributions to particle size, is extracted from a histogram plot of center separations. (f) Plot of effective radius vs ligand length predictions by OPM (red curve) and three-body OCM (blue curve) with experimental data collected from hexagonal monolayers of PbS and Au NCs of 3−5 nm core diameter and C_9- or C_{18}-length ligands. The full widths at half-maximum (fwhm's) of the effective size and core diameter distributions are denoted by vertical and horizontal error bars, respectively.

crystalline self-assembled monolayers (SAMs)[27]), disorder of the capping ligands in NC SLs typically hides such microscopic details in ensemble averages.[28] X-ray scattering has been used to evaluate the contribution of ligands to the overall particle size[29] and, more recently, to reveal the presence of crystalline domains of ligands packed between NC cores in fcc superlattices of oleic acid-capped PbS NCs.[30] In parallel, TEM has found use in real-space imaging of superlattices[10] and single particles[31] with subnanometer resolution. Individual ligand molecules have been revealed by imaging NCs on graphene or suspended over vacuum.[32] While ligand molecules are not visible against the amorphous carbon support used in our experiments, their structure can be indirectly probed by measuring the separation between NC surfaces. Electron beam transmission through the entire sample ensures that measurements collected on multilayer superlattices are representative of bulk dimensions. In addition, tilting of the TEM sample holder allows for three-dimensional reconstruction of the superlattice unit cell. We used software analysis of hundreds of images to collect large data sets (~10^6 individual NCs) and confirm the statistical significance of our results.

To date, two models have been proposed to evaluate the contribution of the soft ligand corona to the effective size of a hydrocarbon-capped NC. In simple analytical form, ligand packing has been reduced to geometric shapes, with a sphere, cylinder, and cone representing the NC core, ligand chain, and explorable space, respectively (Figure 2a). The optimal packing model (OPM)[33] is built on the assumption that the ligands pack densely only within a narrow volume along the contact axis between nearest neighbors (Figure 2b, top) and predicts the interparticle separation to be $R_{eff}/R = (1 + 3L/R)^{1/3}$. An alternative overlap cone model (OCM)[34] assumes that the ligands fill space at the bulk hydrocarbon density within the entire overlap volume (Figure 2b, bottom). For sufficiently soft ($L/R \gtrsim 0.5$) core−ligand combinations, this model predicts that alkane chains completely fill the volume between NC cores and that assemblies of such particles are perfectly space-filling. The OCM assumption of dense ligand packing suggests a shorter separation between NC cores than OPM and predicts the existence of many-body effects, or non-pairwise interactions between ligand capping layers. Some experiments[33] support the accuracy of OPM, while other data and molecular simulations[34] agree with the OCM predictions.

We began our study by establishing how deeply ligand coronas interpenetrate after solvent evaporation and the associated implications for the space-filling efficiency of close-packed NCs. Using several batches of PbS and Au NCs with core diameters varying from 3 to 5 nm, we carried out ligand exchange (Figure S1 in the Supporting Information) to replace the original capping ligands with C_9- and C_{18}-length hydrocarbon chains with carboxylic acid and thiol anchoring groups for PbS and Au NCs, respectively. This allowed us to obtain sets of capped NCs with softness parameters spanning the range $0.50 < L/R < 1.75$. Tetrachloroethylene solutions of these NCs were drop-cast on carbon supports, and many (~25) TEM images of hexagonally arranged NCs at submonolayer coverage were collected for each set (Figure S2). TEM images were analyzed using a MATLAB particle tracking code. Identification of NC cores in the image and connecting their centers produced a hexagonal network of line segments (Figure 2c,d) with lengths corresponding to the effective NC diameters, including core and ligand contributions to the particle size. Plotting a histogram of the measured separations yielded a distribution centered on the effective NC diameter and broadened by some variation in core size and depth of corona overlap (Figure 2e).

For all softness values, the measured average effective NC size was found to fall within 10% of the OPM prediction

DOI: 10.1021/jacs.5b00839
J. Am. Chem. Soc. 2015, 137, 4494−4502

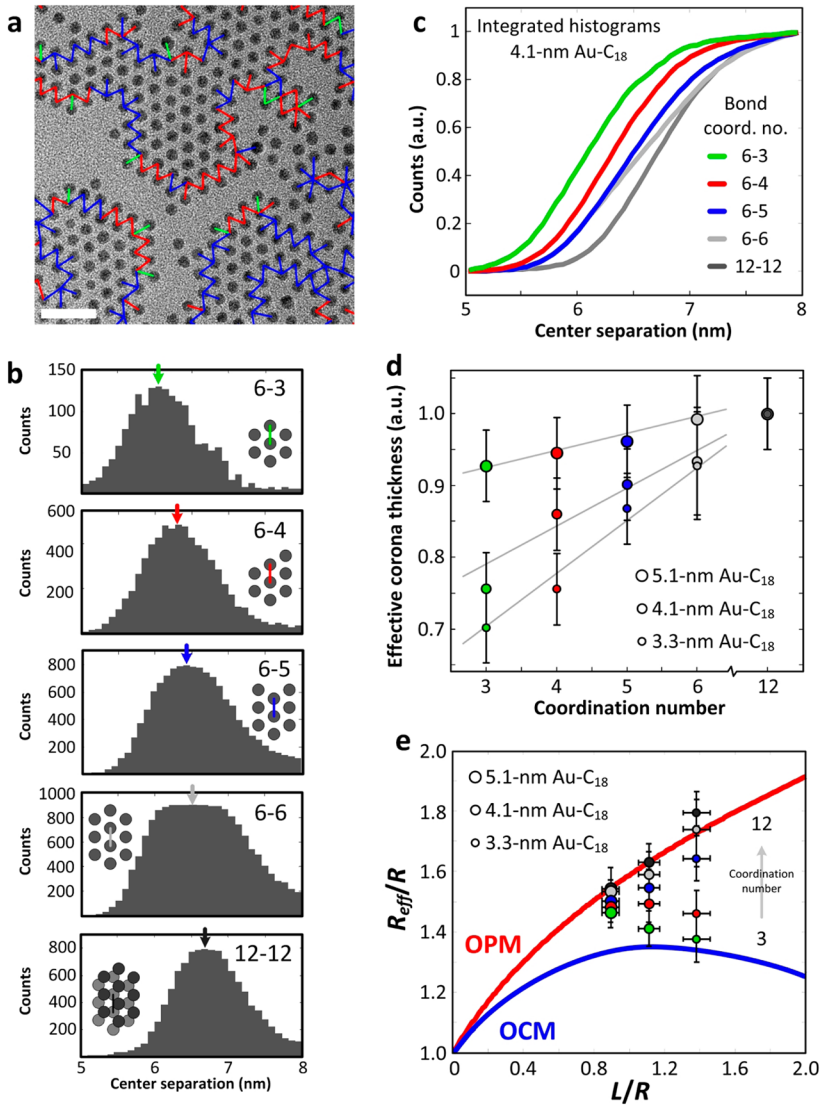

Figure 3. Measurement of coordination-dependent effective nanocrystal size. (a) Sample area of a TEM image of 4.1 nm Au−C_{18} NCs, with 6−3 bonds shown in green, 6−4 bonds in red, 6−5 bonds in blue, and 6−6 bonds omitted for clarity. The scale bar is 20 nm. (b) Extracted interparticle separation statistics for 6−3, 6−4, 6−5, and 6−6 monolayer bonds as well as 12−12 trilayer bonds. Distribution modes marked with arrows. (c) Integration of the histogram plots in (b) allows for comparison of the left edges of the distributions, containing bonds between NCs in closest association. (d) Effective corona thickness vs coordination number for three sizes of Au−C_{18} NCs normalized with respect to surface separation in a multilayer superlattice. Error bars correspond to distribution fwhm's. Gray lines serve to guide the eye. (e) Plot of measured effective NC sizes in R_{eff}−L space, allowing comparison against ligand-packing theories.

(Figure 2f). The three-body OCM solution, on the other hand, systematically underestimated the effective size, most notably for the softest core−ligand combinations ($L/R > 1$). From this observation we conclude that hydrocarbon chains do not completely fill the space between NC cores. Instead, assemblies of organic-capped NCs jam at a separation that leaves ∼1/3 of this volume open (Figure S3). The attraction between hydrocarbon chains (∼4 meV per methylene unit in vacuum[35]) favoring dense packing of segments is opposed by the finite compressibility of entangled, interdigitating chains tethered at one end to an approximately spherical surface. Indeed, with molecular lengths (C_9−C_{18}, 1.2−2.3 nm) on the order of the Kuhn segment (1.4 nm for polyethylene[36]), organic capping ligands may best be described as semiflexible rods with elastic response that precludes liquidlike molecular packing of alkane chains.

Figure 2f shows the measured effective particle size averaged over all contacts in NC films deposited at submonolayer coverage. While most of the particles we imaged were embedded within the array interior, some sat at island edges and had comparatively fewer nearest neighbors (Figure S4). To gain deeper insight into the local structure of NC packings, we used particle tracking to assign each NC a coordination number and categorize the center separations on the basis of the coordination states of the two NC end points (Figure 3a). We found that the coordination number plays an important role in setting the effective NC size: the measured separations between fully coordinated particles are greater than those between particles having open coordination sites. Using 4.1 nm Au−C_{18} NCs as an example, in Figure 3b we demonstrate the expansion of the effective NC size with increasing coordination number by plotting the interparticle separations for the coordination series 6−n, where one NC is fully coordinated in two dimensions and

DOI: 10.1021/jacs.5b00839
J. Am. Chem. Soc. 2015, 137, 4494−4502

the other has coordination number $3 \leq n \leq 6$. We also collect separations for the same Au NCs embedded in hcp trilayers (n = 12), which appear as hexagonal arrays of alternating dark and light NCs (Figure S5).

Taking the distribution maximum to be the true separation, the effective NC size increases with the number of overlaps. To exclude the possibility of size selection on the grid, whereby small NCs are pushed to the superlattice periphery, we measured the core diameters using an edge detection code (Figure S6). We found no change in core size with coordination number, confirming that the variation in effective NC size is a capping ligand effect. We tested the statistical significance of our measurements by calculating the probability that these observed shifts in effective NC size might be attributed to random fluctuations around the typical separation of fully coordinated particles (the P value). This analysis confirmed that the observed effects are significant at the 95% confidence level.[37]

The bond length distributions have positive skew (a long right-side tail) attributed to a population of loosely overlapping NCs. Examining those in close contact on the left side of the distribution enables a meaningful comparison of relaxed interparticle spacings. Integrating the histograms reveals the closest approach for coordinatively unsaturated NCs (Figure 3c). The non-Gaussian shape of the 6−6 distribution may be a consequence of local relaxation of tensile stress by roughening of separations within the interior of islands (Figure S7). We also measured the interparticle separation versus coordination number for 3.3 and 5.1 nm Au−C_{18} NCs (Figure S8) and plotted the results for all three sets of NCs in the same window (Figure 3d). Separations were normalized with respect to the hcp trilayer distance. For 3.3 nm Au−C_{18} NCs ($L/R \approx 1.4$), we found that removing nearest neighbors resulted in a considerable (~30%) reduction of the corona contribution to the effective NC size, while the same effect was much smaller (~6%) for 5.1 nm Au−C_{18} NCs ($L/R \approx 0.9$). Since the van der Waals interaction energy between NC cores scales with particle volume (i.e., should be significantly larger for 5.1 nm Au NCs compared with 3.3 nm NCs), this observation allowed us to exclude core−core attraction as the primary cause of variation in the effective NC size. Plotting the separations on top of the predictions made by the OPM and OCM theories (Figure 3e) revealed that although the measured separations between coordinatively saturated NCs are close to the OPM prediction, much shorter separations are measured for NCs with large L/R and few nearest neighbors. The observed influence of surrounding particles on the state of two contacting particles indicates that the hydrocarbon capping layer supports many-body interactions between NCs that are not anticipated by the pairwise considerations of OPM.

We attribute the many-body effect to deformation of the ligand corona. As particles are brought into contact during solvent evaporation, hydrocarbon chains are concentrated along the central axis between nearest neighbors (Figure 4a, top). This accumulation of ligand segments is accompanied by osmotic pressure pushing solvated chains outward (Figure 4a, bottom). While the corona of a particle embedded within the bulk of a close-packed array experiences nearly uniform pressure from all sides (Figure 4b, top), the corona of a low-coordination particle does not. As a result, the entropic drive to distribute ligand segments uniformly throughout the space between NC cores forces coordinatively unsaturated particles to shift chains away from contacts and allows them to sit closer

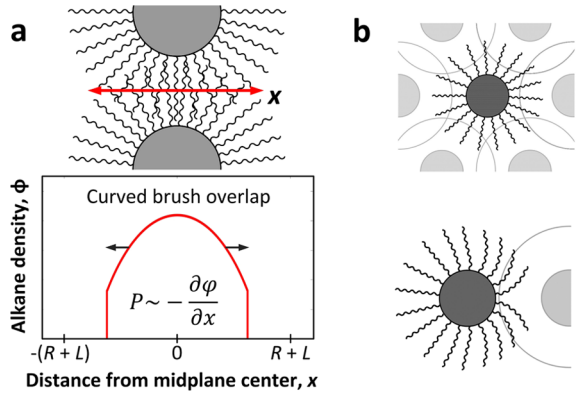

Figure 4. Geometric model of ligand overlap and corona deformation for low-coordination nanocrystals. (a) Overlap of spherical brushes (e.g., nanocrystal coronas) results in accumulation of segments in the center of the midplane. Osmotic pressure at the contact pushes ligands toward the periphery. (b) The corona of a nanocrystal fully surrounded by neighbors (top) experiences nearly uniform pressure from neighboring segments and features an isotropic ligand chain distribution. The corona of a coordinatively unsaturated nanocrystal (bottom) is shifted away from contact and toward solvent-rich void space as a result of the osmotic pressure gradient across the sphere surface.

to their neighbors (Figure 4b, bottom). Indeed, this effect has been anticipated by molecular dynamics (MD) simulations of pairwise interactions between alkanethiol-capped Au NCs[34] and self-consistent-field theory calculations of overlapping spherical brushes.[38]

The capping ligand structure may also be influenced by the amorphous carbon film that supports NCs resting on the TEM grid. MD simulations of Au NCs passivated with dodecanethiol and adsorbed on a graphite surface predicted ligand chains to be tilted away from the graphite surface normal,[39] creating some solid angle of the NC surface in which no chain ends are found. This effect should apply to all NCs in contact with the carbon support (Figures 2c and 3a), and the substrate can be viewed as an additional "neighbor" acting on all of the NCs in the monolayer. We expect that the effect of the coordination environment on the effective NC size shown in Figure 3 should be even stronger for NC assemblies suspended in solution.

With simple geometry and chain-packing assumptions, OPM and OCM are appealing models for considering "hairy" sphere packings. OPM correctly predicts the dimensions of extended NC arrays. On the other hand, this model treats only pairwise interactions between nearest neighbors and thus provides no means to understand the observed many-body interaction. OCM correctly anticipates the many-body effect, but it results from the assumed tendency for alkanes to pack between cores in extended space-filling domains, an assumption that leads to predicted separations that are much shorter than our experimental measurements (Figure 2f). Importantly, the ability of a spherical NC corona to be deformed in response to its surroundings appears to be missing from this analysis to date.

Next, we investigated the role of ligands in binary nanocrystal superlattices (BNSLs). We used ligand exchange to tune the softness of the NC building blocks and the effective radius ratio ($\gamma_{eff} = R_{eff,B}/R_{eff,A}$, with R_{eff} values measured from single-component arrays[10]) for nominally identical NC cores. For example, we assembled BNSLs from 4.1 nm Au and 7.0 nm PbS NCs in two capping ligand combinations: PbS−C_{18} ($L/R \approx 0.65$) and Au−C_9 ($L/R \approx 0.58$), with the two components

DOI: 10.1021/jacs.5b00839
J. Am. Chem. Soc. 2015, 137, 4494−4502

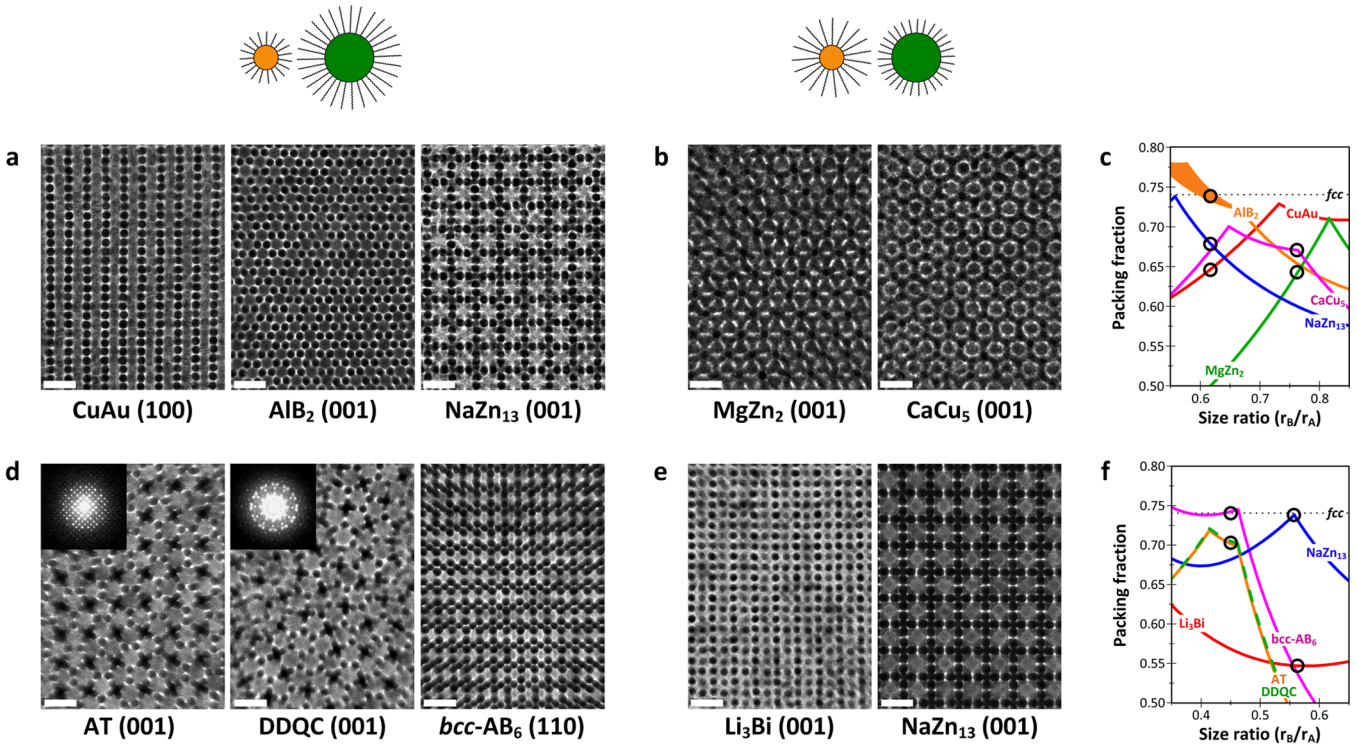

Figure 5. Self-assembly of binary nanocrystal superlattices with different ligand combinations. (a) TEM images of CuAu-, AlB_2-, and $NaZn_{13}$-type BNSL phases formed from evaporation of solutions containing 7.0 nm PbS−C_{18} and 4.1 nm Au−C_9 NCs. (b) TEM images of $MgZn_2$- and $CaCu_5$-type BNSLs formed from PbS−C_9 and Au−C_{18} with the same cores as in (a). A schematic of tailoring the ligand corona thickness is shown above the BNSL images in (a) and (b). (c) Space-filling curves calculated for hard-sphere arrangements of the observed binary structures of PbS and Au NCs. (d) TEM images of $3^2.4.3.4$ Archimedean tiling (AT), dodecagonal quasicrystal (DDQC), and body-centered cubic (bcc) AB_6-type BNSL phases formed from 10.2 nm Fe_2O_3−C_{18} and 4.1 nm Au−C_9 NCs. Insets: electron diffractograms collected from the AT- and DDQC-type BNSLs. (e) TEM images of Li_3Bi- and $NaZn_{13}$-type BNSLs at formed from 10.2 nm Fe_2O_3−C_9 and 4.1 nm Au−C_{18} NCs with the same cores as in (d). (f) Space-filling curves calculated for hard-sphere arrangements of the observed binary structures of Fe_2O_3 and Au NCs. Scale bars are 20 nm.

having similar soft character, and PbS−C_9 ($L/R \approx 0.34$) and Au−C_{18} ($L/R \approx 1.1$), with Au−C_{18} much softer than PbS−C_9. Evaporation of solutions containing Au−C_9 and PbS−C_{18} NCs ($\gamma_{eff} \approx 0.62$) in various concentration ratios reproducibly generated three binary phases: CuAu, AlB_2, and $NaZn_{13}$ (Figure 5a). On the other hand, doing the same with Au−C_{18} and PbS−C_9 ($\gamma_{eff} \approx 0.76$) produced two phases: $MgZn_2$ and $CaCu_5$ (Figure 5b). We modeled the observed BNSLs as rigid-sphere packings and found that only AlB_2 has a density comparable to that of close-packed monodisperse spheres, $\rho_{fcc/hcp} \approx 0.74$ (Figure 5c). This is in line with previous works[22] and highlights the apparent conflict between the entropic preference for dense NC packings and the frequent observation of supposedly open BNSL arrangements.

Similar results were observed for the assembly of a second set of BNSLs from 4.1 nm Au and 10.2 nm γ-Fe_2O_3 building blocks. Cocrystallization of Fe_2O_3−C_{18} ($L/R \approx 0.45$) and Au−C_9 ($L/R \approx 0.58$) NCs ($\gamma_{eff} \approx 0.45$) yielded $3^2.4.3.4$ Archimedean tiling (AT), dodecagonal quasicrystal (DDQC),[13] and body-centered cubic (bcc) AB_6-type[12] BNSLs isostructural with K_6C_{60} (Figure 5d), while the Au−C_{18} ($L/R \approx 1.1$) and Fe_2O_3−C_9 ($L/R \approx 0.24$) combination ($\gamma_{eff} \approx 0.56$) produced Li_3Bi and $NaZn_{13}$ phases (Figure 5e). We note that the Li_3Bi BNSL, constructed by an fcc arrangement of large spheres with small spheres occupying all of the tetrahedral and octahedral sites, was not reported in earlier work on BNSLs. The Li_3Bi structure assignment was made with the assistance of TEM tilting experiments (Figure S9). Modeling of these structures as binary arrangements of hard spheres suggested that AT, DDQC, bcc-AB_6, and $NaZn_{13}$ phases pack with efficiencies close to that of fcc/hcp, while Li_3Bi appears to be a low-density outlier with predicted space-filling fraction $\rho \approx 0.55$ at this size ratio (Figure 5f).

Although electrostatic charging has been offered as a possible explanation for the counterintuitive phase behavior of binary mixtures of colloidal NCs,[22] later studies revealed examples where Coulomb energy is unlikely to be the primary driver of BNSL phase stability. Thus, measurements of electrophoretic mobility of metal and semiconductor NCs indicate that both remain charge-neutral in hydrocarbon (e.g., *n*-decane) solvents while forming low-density BNSL phases.[11] Our observations that adjusting the A:B mixing ratio tunes the BNSL stoichiometry across a wide range (e.g., Figure 5a) and that most NCs on the TEM grid (~90%) are incorporated into binary structures would be difficult to explain by NC charging.

These considerations prompted us to examine the role of the soft capping layer in stabilizing unanticipated BNSL arrangements. For each structure, we collected images of many domains and systematically tilted samples with respect to the electron beam to obtain several crystallographic projections of the same superlattice. We subjected our library of BNSL images to MATLAB particle tracking analysis (Figures S10 and S11) similar to the measurements shown in Figure 2d. This approach enabled three-dimensional reconstruction of the BNSL unit cell and extraction of experimental interparticle separations (Figure S12).

DOI: 10.1021/jacs.5b00839
J. Am. Chem. Soc. 2015, 137, 4494−4502

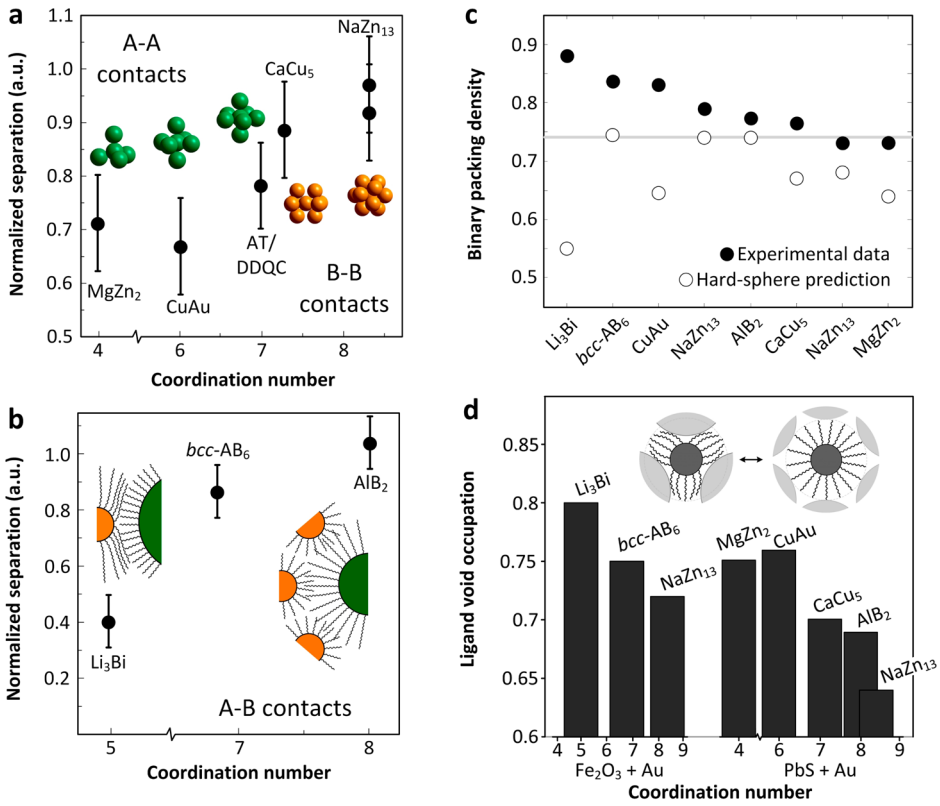

Figure 6. Estimation of experimental interparticle separation, packing density, and ligand void filling in BNSLs. (a) Measurement of NC surface separation in BNSLs with A−A or B−B contacts plotted against coordination number. Each BNSL contact separation is normalized with respect to the separation measured for close-packed monodisperse arrays of the same NCs. Error bars represent fwhm's of the surface separation distributions. The insets show illustrations of the jamming contact geometry for each BNSL structure. (b) Measurement of NC surface separation in BNSLs with A−B contacts vs BNSL coordination number. The insets show illustrations of the proposed collapse of a diffuse corona in contact with a dense corona for Li_3Bi (left) and the spherical symmetry of a corona engaged in crowded contacts (right). (c) Experimental density (solid circles) and density predictions based on hard-sphere models (open circles) for observed BNSL structures. The gray line marks the density of monodisperse close-packed spheres. (d) Experimental estimation of ligand void occupation for BNSLs ordered by average coordination number.[37] The inset shows a sketch of a low-coordination NC with a deformed ligand corona and a high-coordination NC with a spherical effective shape.

To quantify the crowding at NC contacts, we introduced a BNSL coordination number: for BNSLs supported by contacts between A spheres (e.g., PbS−PbS contacts in $MgZn_2$- and CuAu-type structures), the BNSL coordination number was simply taken as the coordination state of A spheres (e.g., 4 for the diamond-type A-sphere sublattice of $MgZn_2$ and 6 for octahedral A-sphere coordination of CuAu). For BNSLs supported by contacts between B spheres (e.g., Au−Au contacts in $CaCu_5$- and $NaZn_{13}$-type structures), the average coordination number of nonequivalent B_1 and B_2 spheres was calculated, weighted by the abundance of each within the BNSL structure.[37] We assigned average coordination numbers of 7.2 for $CaCu_5$-type and 8.3 for $NaZn_{13}$-type BNSLs. For BNSLs supported by A−B contacts (e.g., PbS−Au contacts in AlB_2 and Fe_2O_3−Au contacts in Li_3Bi and bcc-AB_6 BNSLs), the same weighted-average BNSL coordination number was calculated using A- and B-sphere coordination states. We gave Li_3Bi, bcc-AB_6, and AlB_2 BNSLs average coordination numbers of 5, 6.9, and 8, respectively.

We then calculated a normalized separation by dividing the experimental surface-to-surface separation by the separation expected for extended arrays of single-component close-packed NCs (the OPM prediction). This analysis revealed that the NC corona, while nearly spherical when particles are embedded in extended close-packed arrays, can be significantly deformed for particles packed in low-coordination sites. For example, BNSLs supported by an A-sphere framework ($MgZn_2$, CuAu, AT, DDQC) feature PbS or Fe_2O_3 NCs in sites with fewer nearest neighbors (just 4 to 7) than in the 12-coordinate fcc/hcp arrangement. BNSL measurements suggested that these NCs are able to pack more closely together in binary structures, with surface separations ∼65−80% of that for the same particles packed in monodisperse arrays (Figure 6a, left three data points). BNSLs supported by contacting B spheres ($CaCu_5$, $NaZn_{13}$) incorporate Au NCs with fewer nearest neighbors than the fcc/hcp arrangement (∼7−8 vs 12), and these particles also appear to be compressed slightly compared with monodisperse close-packing predictions (Figure 6a, right three data points). BNSLs with A−B contacts (Li_3Bi, *bcc*-AB_6, AlB_2) show the same structure densification resulting from compression of particles with low coordination number (Figure 6b). Most notably, the Li_3Bi-type BNSL incorporating soft Au−C_{18} NCs packed into the tetrahedral voids between hard Fe_2O_3−C_9 NCs appears to squeeze the soft particle corona such that surface separation between the two is less than half that predicted on the basis of OPM and monodisperse array measurements. Analysis of the statistical significance of this measurement allowed us to reject the null hypothesis with 95% confidence.[37]

The sphere-packing considerations typically employed in BNSL structural analysis and the assumption of spherical NC cores employed by OPM and OCM ligand theories overlook

DOI: 10.1021/jacs.5b00839
J. Am. Chem. Soc. 2015, 137, 4494−4502

the additional structural complexity (e.g., orientational registry of NCs within superlattices[40] and facet-selective attachment of NC cores[41]) that may be incorporated into superlattices formed from NCs with patchy interactions contributed by faceted core shape and directional ligand desorption. Nonetheless, this effect appears to play a minor role in the self-assembly of our BNSLs, as only the CuAu-type structure (one of 10 observed here) shows WAED reflections consistent with strong orientational ordering of PbS NCs (Figure S13). We anticipate that the simplifying approximation of spherical NC cores should be valid for structural analysis of superlattices with randomly oriented particles.

DISCUSSION

Variable effective particle size resulting from deformability of the hydrocarbon capping layer brings up an unanticipated connection between NCs and metal ions, whose radii similarly depend on the coordination environment. The Na^+ ion serves as a textbook example: its ionic radius is defined as 0.99, 1.02, 1.18, and 1.39 Å for structures with coordination numbers of 4, 6, 8, and 12, respectively.[42] We extend this analogy between ionic compounds and NC solids by proposing a set of principles for predicting the relative stability of BNSL structures in the style of the Pauling rules for simple salts.[43] These rules expand upon the concepts of sphere packing[6] and complement a different set of rules devised for the unique case where the particles feature strong attraction of complementary DNA ligands during assembly.[44]

Rule 1. *In addition to effective size, a hydrocarbon-capped NC has "softness" (L/R) that determines its ability to adopt the shape of a particular coordination environment.*

The fraction of total particle volume contributed by ligands can be approximated[37] as $V_{lig}/(V_{lig} + V_{core}) \approx (L/R)/(L/R + {}^1/_3)$. Accordingly, for core−ligand combinations with $L/R \gtrsim 0.33$, hydrocarbons represent most of the NC footprint in space. Self-assembly of NCs with minimal softness generally follows the rules of sphere packing. On the other hand, for sufficiently soft NCs, the tendency for ligands to be redistributed away from contacts during colloidal crystallization should be taken into account.

Rule 2. *In a low-coordination site, a soft NC fills space more efficiently than a hard NC because it can adjust its shape to the available space as determined by the local coordination geometry.*

Perturbation of the spherical corona symmetry via deformation of the capping layer always acts to densify the structure by allowing a particle to adopt an effective shape that resembles the Voronoi cell of the lattice site. This geometric distortion changes poorly packing units (for packing in three dimensions, spheres are the least-efficient convex solid known[45]) into a softened version of perfectly packing Voronoi polyhedra.

Rule 3. *Softness stabilizes cocrystallization.*

Although not stated in the original work, it can be easily shown[37] that the OPM interparticle separation results in a predicted packing density for close-packed (fcc) spheres of $\pi/3\sqrt{2} \approx 0.74$ for all L/R values. The agreement between our measurements of extended arrays of close-packed monodisperse NCs and the OPM result (Figure 2f) leads us to the satisfyingly simple conclusion that hydrocarbon-capped spheres, like their hard-sphere counterparts, close-pack at 74% density for all softness values.

We also estimated an experimental packing fraction for the observed binary structures and compared it with the predictions made by rigid-sphere packings (Figure 6c). We found that BNSLs are in fact much denser than sphere-packing models predict, with estimated space-filling fractions of $0.73 < \rho < 0.88$, indicating that cocrystallization does not lead to anomalously open arrangements. As such, while hard and soft particles only fill 74% of space as separately close-packed arrangements of spheres, they can mix together into a dense, low-coordination binary structure that uses deformable spheres to "glue" together the rigid ones.

Structure densification resulting from deformability of soft particle surfaces offers important insight into the thermodynamics of BNSL formation. If BNSL self-assembly is driven by free-volume entropy, two NC species should not mix unless it increases their density. Our observation that cocrystallization does not produce anomalously low density BNSLs indicates that no complex set of distance-dependent energetic interactions need be invoked to explain the formation of BNSLs, though they may play some part in the free energy of BNSL formation. Some binary phases, however, appear to contain slightly more open space than close-packed monodisperse spheres ($NaZn_{13}$, $MgZn_2$; Figure 6c). This allows for the possibility that second-order effects may play a role in favoring mixing of two NC components. Indeed, for binary hard-sphere mixtures, simulations[5] and experiments[46] have suggested that the configurational entropy gain associated with the formation of the $NaZn_{13}$ arrangement is sufficient to stabilize the structure against phase separation for densities as low as ∼0.69 within the size ratio range $0.52 < \gamma < 0.60$. With the additional degrees of freedom offered by reduced spatial ordering of binary crystals compared with phase-separated arrangements, configurational entropy should be sufficient to stabilize the observed BNSLs with estimated density of ∼0.73.

Rule 4. *In stark contrast to ionic solids, soft NC packings prefer low-coordination arrangements, as this geometry allows for the densest packing of ligands between cores.*

We used the measured BNSL dimensions to estimate the space-filling efficiency of ligands between NC cores and found the densest packing of hydrocarbons in low-coordination structures (Figure 6d). This observation can be applied to rationalize the relative stability of plausible BNSL candidate structures at a particular effective size ratio. For example, AlB_2 at $\gamma = 0.56$ has optimal sixfold-coordinated B spheres and the densest packing of all possible binary hard-sphere arrangements. Instead of forming the AlB_2-type arrangement, NCs mixed at $\gamma_{eff} \approx 0.56$ in this work self-assembled into the Li_3Bi structure with fourfold-coordinated Au−C_{18} NCs. Similarly, NaCl at $\gamma = 0.45$ maximally coordinates the B spheres with six nearest neighbors and is the densest binary phase for hard-sphere packings. Instead of forming NaCl, NCs mixed at $\gamma_{eff} \approx 0.45$ yielded bcc-AB_6, with fourfold-coordinated B spheres. Once more, instead of CuAu-type BNSLs, the densest binary sphere arrangement at $\gamma = 0.76$, $MgZn_2$ and $CaCu_5$ are found. In these structures, the B spheres form a network of vertex-sharing trigonal bipyramids with fewer nearest-neighbor contacts than the optimal eightfold-coordinated B spheres of CuAu.

Dense packing of soft particles in low-coordination lattice sites, as demonstrated in this work by TEM measurements, has also been shown in a SAXS study of oleic acid-capped PbS NC assemblies, which were found to fill space more efficiently in the bcc polymorph than in the fcc polymorph.[47] This idea might naturally explain the fcc-to-bcc phase transition observed for alkanethiolate-capped Au NCs for $L/R > 0.7$[20] and the fact

DOI: 10.1021/jacs.5b00839
J. Am. Chem. Soc. 2015, 137, 4494−4502

that "softening" of NCs by incorporation of organic guest molecules (e.g., squalane) into the capping layer produces a similar fcc-to-bcc transition for PbSe NCs.[48]

CONCLUSIONS

This work has characterized the contribution of surface ligands to the self-assembly of NC superlattices. We have laid the conceptual foundation for describing dense arrangements of deformable spheres and used it to rationalize the complex zoo of BNSL phases as entropy-driven crystallization of soft objects. We anticipate that these findings should apply to other deformable objects (e.g., micelles, vesicles, and globular proteins).

ASSOCIATED CONTENT

Supporting Information

TEM images, FTIR spectra, superlattice modeling, particle tracking measurements, sample calculations, and supplementary discussions. This material is available free of charge via the Internet at http://pubs.acs.org.

AUTHOR INFORMATION

Corresponding Author

*dvtalapin@uchicago.edu

Notes

The authors declare no competing financial interest.

ACKNOWLEDGMENTS

We thank W. T. M. Irvine for providing a kernel of particle tracking code, T. Witten for helpful discussions, and S. Rupich for providing iron oxide nanocrystals. This work was supported by the NSF MRSEC Program under Award DMR-1420709 and by the Air Force Office of Scientific Research under Grant FA9550-14-1-0367. D.V.T. also thanks the Keck Foundation and the II−VI Foundation for support.

REFERENCES

(1) Sanders, J. V. *Nature* **1964**, *204*, 1151.
(2) Pusey, P. N.; van Megen, W. *Nature* **1986**, *320*, 340.
(3) Hunt, N.; Jardine, R.; Bartlett, P. *Phys. Rev. E* **2000**, *62*, 900.
(4) Sanders, J. V. *Philos. Mag. A* **1980**, *42*, 705.
(5) Eldredge, M. D.; Madden, P. A.; Frenkel, D. *Nature* **1993**, *365*, 35.
(6) Murray, M. J.; Sanders, J. V. *Philos. Mag. A* **1980**, *42*, 721.
(7) Bartlett, P.; Ottewill, R. H.; Pusey, P. N. *Phys. Rev. Lett.* **1992**, *68*, 3801.
(8) Ben-Simon, A.; Eshet, H.; Rabani, E. *ACS Nano* **2013**, *7*, 978.
(9) Leunissen, M. E.; Christova, C. G.; Hynninen, A.-P.; Royall, C. P.; Campbell, A. I.; Imhof, A.; Dijkstra, M.; van Roij, R.; van Blaaderen, A. *Nature* **2005**, *437*, 235.
(10) Shevchenko, E. V.; Talapin, D. V.; Murray, C. B.; O'Brien, S. *J. Am. Chem. Soc.* **2006**, *128*, 3620.
(11) Bodnarchuk, M. I.; Kovalenko, M. V.; Heiss, W.; Talapin, D. V. *J. Am. Chem. Soc.* **2010**, *132*, 11967.
(12) Ye, X.; Chen, J.; Murray, C. B. *J. Am. Chem. Soc.* **2011**, *133*, 2613.
(13) Talapin, D. V.; Shevchenko, E. V.; Bodnarchuk, M. I.; Ye, X.; Chen, J.; Murray, C. B. *Nature* **2009**, *461*, 964.
(14) Evers, W. H.; De Nijs, B.; Filion, L.; Castillo, S.; Dijkstra, M.; Vanmaekelbergh, D. *Nano Lett.* **2010**, *10*, 4235.
(15) Chen, Z.; O'Brien, S. *ACS Nano* **2008**, *2*, 1219.
(16) Murray, C. B.; Norris, D. J.; Bawendi, M. G. *J. Am. Chem. Soc.* **1993**, *115*, 8706.
(17) Leff, D. V.; Brandt, L.; Heath, J. R. *Langmuir* **1996**, *12*, 4723.
(18) Hyeon, T.; Lee, S. S.; Park, J.; Chung, Y.; Na, H. B. *J. Am. Chem. Soc.* **2001**, *123*, 12798.
(19) Murray, C. B.; Kagan, C. R.; Bawendi, M. G. *Science* **1995**, *270*, 1335.
(20) Whetten, R. L.; Shafigullin, M. N.; Khoury, J. T.; Schaaff, T. G.; Vezmar, I.; Alvarez, M. M.; Wilkinson, A. *Acc. Chem. Res.* **1999**, *32*, 397.
(21) Kiely, C. J.; Fink, J.; Brust, M.; Bethell, D.; Schiffrin, D. J. *Nature* **1998**, *396*, 444.
(22) Shevchenko, E. V.; Talapin, D. V.; Kotov, N. A.; O'Brien, S.; Murray, C. B. *Nature* **2006**, *439*, 55.
(23) Talapin, D. V. *ACS Nano* **2008**, *2*, 1097.
(24) Talapin, D. V.; Shevchenko, E. V.; Murray, C. B.; Titov, A. V.; Král, P. *Nano Lett.* **2007**, *7*, 1213.
(25) Peng, S.; Lee, Y.; Wang, C.; Yin, H.; Dai, S.; Sun, S. *Nano Res.* **2008**, *1*, 229.
(26) Hines, M. A.; Scholes, G. D. *Adv. Mater.* **2003**, *15*, 1844.
(27) Laibinis, P. E.; Whitesides, G. M.; Allara, D. L.; Tao, Y. T.; Parikh, A. N.; Nuzzo, R. G. *J. Am. Chem. Soc.* **1991**, *113*, 7152.
(28) Badia, A.; Cuccia, L.; Demers, L.; Morin, F.; Lennox, R. B. *J. Am. Chem. Soc.* **1997**, *119*, 2682.
(29) Korgel, B. A.; Fullam, S.; Connolly, S.; Fitzmaurice, D. *J. Phys. Chem. B* **1998**, *102*, 8379.
(30) Wang, Z.; Schliehe, C.; Bian, K.; Dale, D.; Bassett, W. A.; Hanrath, T.; Klinke, C.; Weller, H. *Nano Lett.* **2013**, *13*, 1303.
(31) Zheng, H.; Smith, R. K.; Jun, Y.; Kieselowski, C.; Dahmen, U.; Alivisatos, A. P. *Science* **2009**, *324*, 1309.
(32) Panthani, M. G.; Hessel, C. M.; Reid, D.; Casillas, G.; Jose-Yacaman, M.; Korgel, B. A. *J. Phys. Chem. C* **2012**, *116*, 22463.
(33) Landman, U.; Luedtke, W. D. *Faraday Discuss.* **2004**, *125*, 1.
(34) Schapotschnikow, P.; Vlugt, T. J. H. *J. Chem. Phys.* **2009**, *131*, No. 124705.
(35) Salem, L. *J. Chem. Phys.* **1962**, *37*, 2100.
(36) Rubinstein, M.; Colby, R. *Polymer Physics*; Oxford University Press: New York, 2003.
(37) Details are available in the Supporting Information.
(38) Matsen, M. W. *Macromolecules* **2005**, *38*, 4525.
(39) Luedtke, W. D.; Landman, U. *J. Phys. Chem.* **1996**, *100*, 13323.
(40) Li, R.; Bian, K.; Hanrath, T.; Bassett, W. A.; Wang, Z. *J. Am. Chem. Soc.* **2014**, *136*, 12047.
(41) Boneschanscher, M. P.; Evers, W. H.; Geuchies, J. J.; Altanzis, T.; Goris, B.; Rabouw, F. T.; van Rossum, S. A. P.; van der Zant, H. S. J.; Siebbeles, L. D. A.; Van Tendeloo, G.; Swart, I.; Hilhorst, J.; Petukhov, A. V.; Bals, S.; Vanmaekelberg, D. *Science* **2014**, *344*, 1377.
(42) Shannon, R. *Acta Crystallogr., Sect. A* **1976**, *32*, 751.
(43) Pauling, L. *J. Am. Chem. Soc.* **1929**, *51*, 1010.
(44) Macfarlane, R. J.; Lee, B.; Jones, M. R.; Harris, N.; Schatz, G. C.; Mirkin, C. A. *Science* **2011**, *334*, 204.
(45) Kallus, Y. *Adv. Math.* **2014**, *264*, 355.
(46) Eldridge, M. D.; Madden, P. A.; Pusey, P. N.; Bartlett, P. *Mol. Phys.* **1995**, *84*, 395.
(47) Bian, K.; Wang, Z.; Hanrath, T. *J. Am. Chem. Soc.* **2012**, *134*, 10787.
(48) Nagaoka, Y.; Chen, O.; Wang, Z.; Cao, Y. C. *J. Am. Chem. Soc.* **2012**, *134*, 2868.

DOI: 10.1021/jacs.5b00839
J. Am. Chem. Soc. 2015, 137, 4494−4502